RARE METALS

ORIGINAL ARTICLE

In situ scattering study of multiscale structural evolution during liquid–liquid phase transition in Mg-based metallic glasses

Kang-Hua Li, Jia-Cheng Ge, Si-Nan Liu, Shu Fu, Zi-Xuan Yin, Wen-Tao Zhang, Guo-Xing Chen, Shao-Chong Wei* , **Hua Ji, Tao Feng, Qi Liu*** , **Xun-Li Wang, Xiao-Bing Zuo, Yang Ren, Horst Hahn, Si Lan***

K.-H. Li, J.-C. Ge, S.-N. Liu, S. Fu, Z.-X. Yin, W.-T. Zhang, T. Feng, S. Lan*
Herbert Gleiter Institute of Nanoscience, School of Materials Science and Engineering, Nanjing University of Science and Technology, Nanjing 210094, China
e-mail: lansi@njust.edu.cn

G.-X. ChenS.-C. Wei*, H. Ji
Suzhou Nuclear Power Research Institute Co., Ltd, Suzhou 215004, China
e-mail: weishaochong@cgnpc.com.cn

H. Ji
Key Laboratory of Advanced Materials (MOE), School of Materials Science and Engineering, Tsinghua University, Beijing 100084, China

Q. Liu*, X.-L. Wang
Department of Physics, City University of Hong Kong, Hong Kong 999077, China
e-mail: qiliu63@cityu.edu.hk

Q. Liu, X.-L. Wang
Center for Neutron Scattering, City University of Hong Kong Shenzhen Research Institute, Shenzhen 518057, China

X.-B. Zuo, Y. Ren
X-Ray Sciences Division, Argonne National Laboratory, Lemont, IL 60439, USA

H. Hahn
Institute of Nanotechnology, Karlsruhe Institute of Technology (KIT), Eggenstein-Leopoldshafen 76344, Germany

Abstract The glass-forming ability of Mg–Cu–Gd alloys could be significantly promoted with the addition of Ag. A calorimetric anomaly could be observed in the supercooled liquid region of the Mg–Cu–Ag–Gd metallic glass, indicating the occurrence of a liquid-state phase transition driven by entropy. However, the underlying mechanism of the polyamorphous phase transition remains unsettled. In the paper, in situ scattering techniques were employed to reveal multiscale structure evidence in a $Mg_{65}Cu_{15}Ag_{10}Gd_{10}$ metallic glass with an anomalous exothermic peak upon heating. Resistivity measurements indicate a reentrant behavior for the Mg–Cu–Ag–Gd metallic glass in the anomalous exothermic peak temperature region during heating. In situ synchrotron diffraction results revealed that the local atomic structure tends to be ordered and loosely packed first, followed by reentering into the initial state upon heating. Moreover, time-resolved small-angle synchrotron X-ray scattering (SAXS) results show an increase in nanoscale heterogeneity first followed by a reentrant supercooled liquid behavior. A core–shell structure model has been used to fit the SAXS profiles when polyamorphous phase transition occurs. In contrast, there is no structure anomaly for the reference Mg–Cu–Gd alloy system. The detailed multiscale structural evidence suggests the occurrence of a liquid–liquid phase transition followed by a reentrant behavior in the Mg–Cu–Ag–Gd metallic glass. Our results deepen the understanding of the structural origin of the glass-forming ability and shed light on the possibility of tuning the physical and mechanical properties by heat-treatment in the supercooled liquid region of Mg-based metallic glasses.

Keywords Metallic glasses; Anomalous exothermal peak; Polyamorphous transition; Synchrotron scattering

1 Introduction

Liquid-to-liquid phase transitions (LLPT) belong to the group of polyamorphous phase transitions (PPT) and are driven by entropy, which refers to transitions between

liquid phases with different locally favored structures (LFSs) and identical chemical composition [1–3]. LLPTs have been reported to exist in a number of liquids, such as SiO_2 [4], Ce [5], $Al_2O_3–Y_2O_3$ [6], and triphenyl phosphite (TPP) [7]. High-pressure-induced LLPTs have been frequently reported. Katayama et al. [8] found two forms of liquids with different structures in phosphorus by in situ high-pressure X-ray diffraction (XRD). A similar finding was also observed by neutron diffraction of water [9] with the application of appropriate pressures. It was found that PPT occurred in Ce-Al metallic glasses (MGs) under high pressure, and 4f electron delocalization was proposed to explain the phenomenon [2, 10].

The structural origin of LLPT remains an ambiguous and highly controversial issue due to the interruption of crystallization in the undercooled metallic liquids upon heating/cooling [11]. LLPT was proposed to occur in some glass-forming metallic liquids above the melting point, such as La-based MGs [12]. However, the structural evolution induced by temperature-induced LLPT is more pronounced and may be overlooked in the undercooled liquids when crystallization occurs during cooling [8, 13]. An electrostatic levitation experiment was firstly adopted by Li et al. [14] to demonstrate the possible LLPT in MGs by measuring the change in specific volume during heating and cooling. Later, evidence for LLPT was also found in the glass-forming liquid of Vit1 ($Zr_{42.6}Ti_{12.4}Cu_{11.2}Ni_{10}Be_{23.8}$) [15], $Zr_{50}Cu_{40}Al_{10}$ [16], Vit106 ($Zr_{57}Nb_5Al_{10}Cu_{15.4}Ni_{12.6}$) [13], etc.

Recently, Pham et al. [17] and Lan et al. [18] found that Pd–Ni–P glass alloys with an anomalous exothermic peak (AEP) in the supercooled liquid region underwent a hidden LLPT and subsequent reentrant behavior in the supercooled liquid region (SCL). By using in situ synchrotron XRD experiment, a noticeable change of the atomic structure of the Pd–Ni–P MG was observed in the medium-range scale at a transition temperature (T_C). Moreover, by using small-angle neutron scattering (SANS), the existence of two different liquid states in the supercooled liquid region was proven. Later on, such evidence of hidden LLPT was also observed in Fe–Nb–Y–B MGs [19] and BAM 11 ($Zr_{52.5}Cu_{17.9}Ni_{14.6}Al_{10}Ti_5$) [20]. Therefore, the controversy related to LLPT in MGs can be resolved by using state-of-the-art multiple-scale structure probing techniques on glassy alloys exhibiting an AEP. In addition to the above-mentioned alloy systems, AEP has been found in the calorimetric curves of many other MGs, such as Cu–Zr–Al–Y [21], Gd-Zr–Al–Ni [22] and Mg–Cu–Ag–Gd [23].

Mg-based MGs, as high-strength light alloys combined with excellent corrosion resistance [24–27], have been of great interest to researchers due to their potential applications in hydrogen storage [28] and biomedical [29–31].

Tailoring the atomic-to-nano-microstructure in Mg-based metallic glasses should be helpful in the above applications. However, the limited glass-forming ability (GFA) hindered the application of Mg-based glassy alloys [32]. Previous studies have reported that the GFA of $Mg_{65}Cu_{25}Gd_{10}$ ternary alloys could be significantly improved [33, 34] with Ag substitution for Cu [35]. Although much effort has been made, the structural origin of the enhanced GFA by Ag addition remains unsettled. Moreover, a calorimetric anomaly could often be observed in some Mg–Cu–Ag–Gd MGs in the supercooled liquid region, e.g., $Mg_{65}Cu_{15}Ag_{10}Gd_{10}$ alloy, indicating the occurrence of structure evolution driven by entropy. The hidden liquid-state phase transition opens a possible window to reveal the correlation between the structure evolution and the GFA of Mg–Cu–Ag–Gd alloys.

In this paper, by combining in situ synchrotron XRD and small-angle X-ray scattering (SAXS), the multiscale structural changes were probed in Mg–Cu–Ag–Gd MGs of an AEP during heating. It has been found that LLPT occurs in the supercooled liquid region as temperature rises, accompanied by a change in packing density at T_C. The synchrotron diffraction shows that the local order increases first and reenters into the initial states in the AEP temperature region upon heating. Moreover, the SAXS results indicate that the nanoscale heterogeneous structures appear first and diminish during the following heating process. A core–shell model was applied to analyze the new hidden amorphous structure after the occurrence of LLPT. There is no anomalous structure and property change for the reference alloys Mg–Cu–Gd without an AEP. It was also found that the square resistivity and mechanical properties could be tailored by applying appropriate heat-treatment in the AEP temperature region. Our results suggest that the anomalous multiscale structure evolution may be correlated with the excellent GFA for the Mg–Cu–Ag–Gd MGs of a calorimetric anomaly.

2 Experimental

In this paper, the $Mg_{65}Cu_{15}Ag_{10}Gd_{10}$ and $Mg_{65}Cu_{25}Gd_{10}$ MGs ribbons were prepared using melt-spinning. The master alloys were prepared by induction melting Mg, Cu, Ag, Gd (purity > 99.9%) raw material particles under a high-purity Ti-gettered Argon (Ar) atmosphere. Subsequently, the ribbon samples were produced by the single-roller spinning technique. The thickness of the obtained ribbon is about 45 μm, and the width is 3 mm. XRD (Bruker-AXS D8 Advance) was used to check whether the as-prepared melt-spun ribbons are amorphous. The incident wavelength of the XRD is 0.154 nm, and the range of diffraction angle (2θ) is 20°–60°.

Transmission electron microscopy (TEM, FEI TECNAL G2 20) was also employed to observe the amorphous nature of the sample. A cryogenic ion-miller (Gatan 695C) was used to thin the ribbons using parameters at the beginning: 8° in angle, 8 keV in incident ion beam energy within 25 min in duration time. In order to acquire a better quality of the thin area, proper thinning parameters with a lower angle and lower energy were used: 3° in angle, 3 keV in energy, and 15 min in duration time.

The specific heat capacity experiment of the ribbons of 20 mg in mass was carried out by differential scanning calorimetry (DSC, METTLER TOLEDO) in the high-purity N_2 atmosphere. The N_2 flow rate was 50 ml·min^{-1}. A sapphire reference sample was used for the specific heat capacity (C_p) measurements. The temperature range was set as 323–523 K at a heating rate of 10 K·min^{-1}.

Time-resolved SAXS measurements were conducted at beamline 12-ID of the advanced photon source (APS), Argonne National Laboratory (ANL). The high energy X-ray beam size is 200 μm ×40 μm and wavelength is 0.0886 nm. A high-energy X-ray beam was employed in transmission geometry for data collection. The data rate is ~ 1 Hz. Small-angle scattering data were corrected for background scattering (empty sample holder), transmission and detector efficiency, and set to absolute units. The results were analyzed with the Igor Pro 6 equipped with an IRENA software package [36] to get information on their structure [37].

High-energy synchrotron X-ray diffraction measurements were performed at beamline 11-ID-C of the Advanced Photon Source (APS), Argonne National Laboratory. High energy X-rays with a beam size of 500 μm × 500 μm and wavelength of 0.01173 nm were used for data collection. Two-dimensional (2D) diffraction patterns were obtained using a Perkin Elmer amorphous silicon detector. A Hz data rate was used and the sample to detector distance was 1800 mm. The static structure factor, $S(Q)$, was derived from the 2D diffraction ring patterns recorded on the detector by masking bad pixels, integrating images, subtracting the appropriate background and correcting for oblique incidence, absorption, multiple scattering, and fluorescence. Compton scattering and Laue correction48 was conducted using Fit2D and PDFgetX2 [38].

For the in situ heating square resistance test, before experiments, the surface of the $Mg_{65}Cu_{15}Ag_{10}Gd_{10}$ melt-spun ribbons was polished and cleaned with alcohol to obtain an oxide-free sample surface. Using this procedure, detrimental effects on the resistance measurements could be avoided. A commercial four-point resistance tester with heating furnace equipment was used to measure the square resistance. Before the experiment, the oxide layer on the resistance tester probe has been carefully polished to reduce resistance measurement error. The annealing temperature range is from 303 to 503 K at a heating rate of 10 K·min^{-1}. The resistance tester probe distance is 4 mm. Argon gas was introduced throughout the test to eliminate the error on the resistance value caused by oxidation of the sample during the heating process.

The nanoindentation tests were carried out at room temperature using an Agilent Nano Indenter G200 with a typical Berkovich diamond indenter [39]. Ribbons were made into 3 mm × 3 mm square sheets and heat-treated at different temperatures in DSC. Before the actual experiments, calibrations were conducted on a fused silica standard. The nanoindentation tests were performed to measure the hardness and elastic modulus of $Mg_{65}Cu_{15}Ag_{10}Gd_{10}$ melt-spun ribbons. The load increased from 0 to 20 mN at a loading rate of 0.05 mN·s^{-1}, and the peak load was held for 10 s and then was unloaded at a similar rate with the loading one. To ensure accuracy and eliminate scattering of the indentation data, at least 5 indents for each ribbon were performed during the experiment.

3 Results and discussion

3.1 Thermal-physical behavior and initial sample inspections

Figure 1a shows the specific heat capacity (C_p) curves of two glassy ribbons, $Mg_{65}Cu_{15}Ag_{10}Gd_{10}$ and $Mg_{65}Cu_{25}Gd_{10}$, respectively. The corresponding thermo-physical parameters, i.e., glass transition (T_g), crystallization temperature (T_x), have been labeled in DSC curve. The experiment determined the glass transition temperature of $T_g \sim 441$ K and crystallization temperature of $T_x \sim 453$ K for $Mg_{65}Cu_{15}Ag_{10}Gd_{10}$ and $T_g \sim 412$ K and $T_x \sim 460$ K For $Mg_{65}Cu_{25}Gd_{10}$. There is an AEP in the DSC curve, which is ~ 12 K below the crystallization temperature (T_x), and the temperature is labeled as $T_C \sim 441$ K for $Mg_{65}Cu_{15}Ag_{10}Gd_{10}$ MG. There is no such DSC anomaly for $Mg_{65}Cu_{25}Gd_{10}$. The calculated GFA indicators, the reduced glass transition temperature (T_{rg}, and $T_{rg}=T_g/T_1$) [40, 41] and Gamma value (γ) [42], for both MGs, were calculated and are summarized in Table 1. The upper temperature values of the melting endotherms were measured and are designated by T_1 and summarized in Table 1. The values of GFA indicators for $Mg_{65}Cu_{15}Ag_{10}Gd_{10}$ glass are larger than those of $Mg_{65}Cu_{25}Gd_{10}$ glass, and it is consistent with the larger critical casting thickness of Mg–Cu–Ag–Gd.

The inset in Fig. 1a shows XRD patterns for both MGs. Only broad diffusely scattering peaks for both MGs can be observed, confirming the amorphous characteristic. Figure 1b is the bright-field TEM image for $Mg_{65}Cu_{15}Ag_{10}Gd_{10}$ ribbons, showing no nanoscale
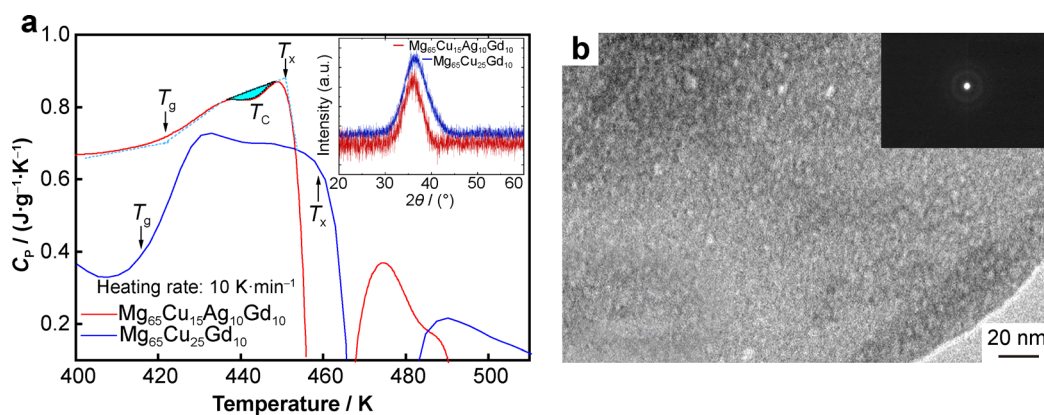
Fig. 1 **a** Specific heat capacity curves C_p for $Mg_{65}Cu_{15}Ag_{10}Gd_{10}$ and $Mg_{65}Cu_{25}Gd_{10}$ MGs and (inset) corresponding XRD patterns; **b** TEM result and SAED pattern (inset) for $Mg_{65}Cu_{15}Ag_{10}Gd_{10}$

Table 1 Thermophysical parameters of $Mg_{65}Cu_{15}Ag_{10}Gd_{10}$ and $Mg_{65}Cu_{25}Gd_{10}$ alloys

Alloys	T_g/K	T_C/K	T_x/K	T_l/K	T_{rg}	γ
$Mg_{65}Cu_{15}Ag_{10}Gd_{10}$	421	441	453	701	0.601	0.404
$Mg_{65}Cu_{25}Gd_{10}$	412	–	460	740	0.557	0.399

precipitate. Moreover, the inset in Fig. 1b is the corresponding selected area electron diffraction (SAED) pattern. The SAED pattern shows diffused halos, further confirming that the samples are amorphous.

### 3.2 In situ synchrotron X-ray diffraction and square resistance measurements results

Figure 2a, b shows the results of in situ synchrotron XRD results of two Mg-based MGs during heating. Both samples show essential amorphous characteristics, that is, diffused peak maxima, upon heating up to T_x. The inset in Fig. 2a is the 2D plot of structure factor $S(Q)$ for $Mg_{65}Cu_{15}Ag_{10}Gd_{10}$. The $S(Q)$ patterns during heating reveal the atomic-scale structural changes. One can observe that the peak position, peak width, and peak intensity for the first sharp diffraction peak between 20 and 30 nm^{-1}, i.e., Q_1, changes between T_g and T_x for the $Mg_{65}Cu_{15}Ag_{10}Gd_{10}$ MG, indicating the occurrence of liquid-state phase transition in the supercooled liquid region. It can be seen that the peak shifts back and forth, and the peak intensity increases first and decreases at a higher temperature around T_C. In contrast, there is no noticeable structure change for the reference sample $Mg_{65}Cu_{25}Gd_{10}$ up to heating above T_x.

To further reveal the evidence of liquid-state phase transition for $Mg_{65}Cu_{15}Ag_{10}Gd_{10}$ MG, Fig. 2c, d shows the first moment vs. temperature curves during heating for both MGs. The first moment represents the peak position of Q_1

[13, 18, 19]. The specific heat capacity (C_p) curves of two ribbons, $Mg_{65}Cu_{15}Ag_{10}Gd_{10}$ and $Mg_{65}Cu_{25}Gd_{10}$ were superimposed. In Fig. 2c, one can find that the peak position firstly decreases and then increases back to the initial value around T_C during the heating process, showing a good correlation with C_P changing in $Mg_{65}Cu_{15}Ag_{10}Gd_{10}$. These anomalous structural changes may point to the LLPT, revealing the existence of hidden metastable amorphous phase in the supercooled liquid region of $Mg_{65}Cu_{15}Ag_{10}Gd_{10}$. The peak position is positively correlated with the packing density of amorphous alloys [43]. The peak intensity correlates positively with the local ordering for the amorphous matters [44]. Therefore, the new amorphous structure becomes more ordered after LLPT, and its packing density would be lower than that of the initial state. To distinguish it from supercooled liquid 1 (SCL1), which occurs around the supercooled liquid region, the new metastable phase is named SCL2. In Fig. 2d, as for the $Mg_{65}Cu_{25}Gd_{10}$ MG, the first-moment curve of Q_1 shows a sharply upward trend at the crystallization temperature (T_x). However, there is no anomalous structure change from T_g to T_x for $Mg_{65}Cu_{25}Gd_{10}$ MG.

The synchrotron diffraction results suggest an LLPT in the supercooled liquid region of the $Mg_{65}Cu_{15}Ag_{10}Gd_{10}$ MG, and the new amorphous phase would dissolve when heated to temperatures higher than T_C, thereby, reentering the supercooled liquid of the room temperature-glass phase. Reentrant has been used to describe this phenomenon in previous studies [45], which refers to a phenomenon in which matter changes back to the original phase after changing from one phase to another [17, 46, 47]. When $Mg_{65}Cu_{15}Ag_{10}Gd_{10}$ metallic glass is heated above the glass transition temperature (T_g), it reaches the initial liquid state SCL1. As the temperature rises, it transforms into a liquid SCL2 with a high degree of order and finally re-transforms to a supercooled liquid
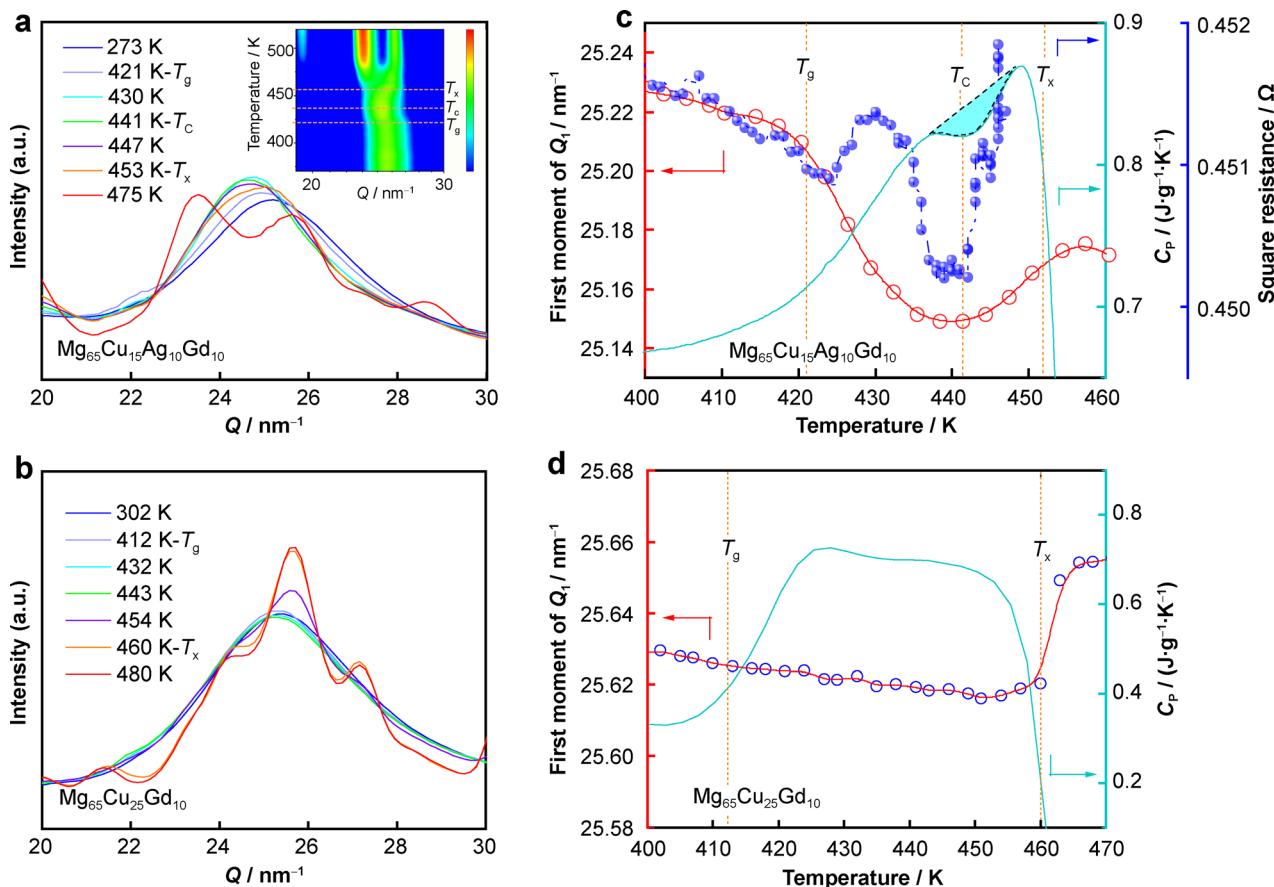
Fig. 2 Synchrotron XRD patterns during heating for **a** $Mg_{65}Cu_{15}Ag_{10}Gd_{10}$ and **b** $Mg_{65}Cu_{25}Gd_{10}$; the first moment of Q_1 (peak position) versus temperature curves for **c** $Mg_{65}Cu_{15}Ag_{10}Gd_{10}$ and **d** $Mg_{65}Cu_{25}Gd_{10}$ MGs, where specific heat versus temperature curves were superimposed

similar to the initial liquid SCL1. This process is similar to the reentrant phenomenon described above.

As shown in Fig. 2c, the square resistance curve of $Mg_{65}Cu_{15}Ag_{10}Gd_{10}$ also displays an abnormal evolution as temperature rises. It is observed that with temperature increasing from room temperature to T_g, the square resistance decreases linearly and slowly. Above the glass transition temperature, the $Mg_{65}Cu_{15}Ag_{10}Gd_{10}$ amorphous alloy undergoes a glass transition into a supercooled liquid state with the change in the relaxation mechanism causing an evolution of the electron transport properties. The square resistance deviates from the original linear relationship and enters another stage; a sharp increase can be observed, as shown in the blue line. As the temperature continues to rise near T_C, the LLPT gradually occurs in the supercooled liquid region, and the square resistance exhibits a downward trend again. As the phase transition further evolves, the resistance rises subsequently. The square resistance curve and DSC curve show a remarkably consistent trend, implying that the in situ resistance method can detect the characteristic temperature of the structural transformation of $Mg_{65}Cu_{15}Ag_{10}Gd_{10}$ amorphous alloy

during heating as well. It can be seen that the square resistance as a physical parameter can reflect the change in the amorphous structure from the electronic level [48–53].

3.3 Time-resolved SAXS

Figure 3a, b shows the results of time-resolved SAXS results of two Mg-based MGs during heating in order to reveal the evolution of nanoscale inhomogeneities and to provide further evidence for reentrant phenomena. The evolution of nanoscale structural heterogeneities matches well with atomic-scale structural changes, further indicating the occurrence of LLPT and the associated reentrant behavior in the supercooled liquid region for the $Mg_{65}Cu_{15}Ag_{10}Gd_{10}$ MG. Unlike $Mg_{65}Cu_{25}Gd_{10}$ MG, one can clearly observe that the SAXS intensity within the range of 1.2–1.7 nm^{-1} shows a rise and fall around T_C of $Mg_{65}Cu_{15}Ag_{10}Gd_{10}$ MGs. Moreover, as shown in Fig. 3c, the integration over the Q range of 1.42–1.53 nm^{-1} instead of the integration over the full Q range shows a rise and fall with T_C temperature, suggesting that a hidden amorphous phase with size of ~ 4 nm first appears and then
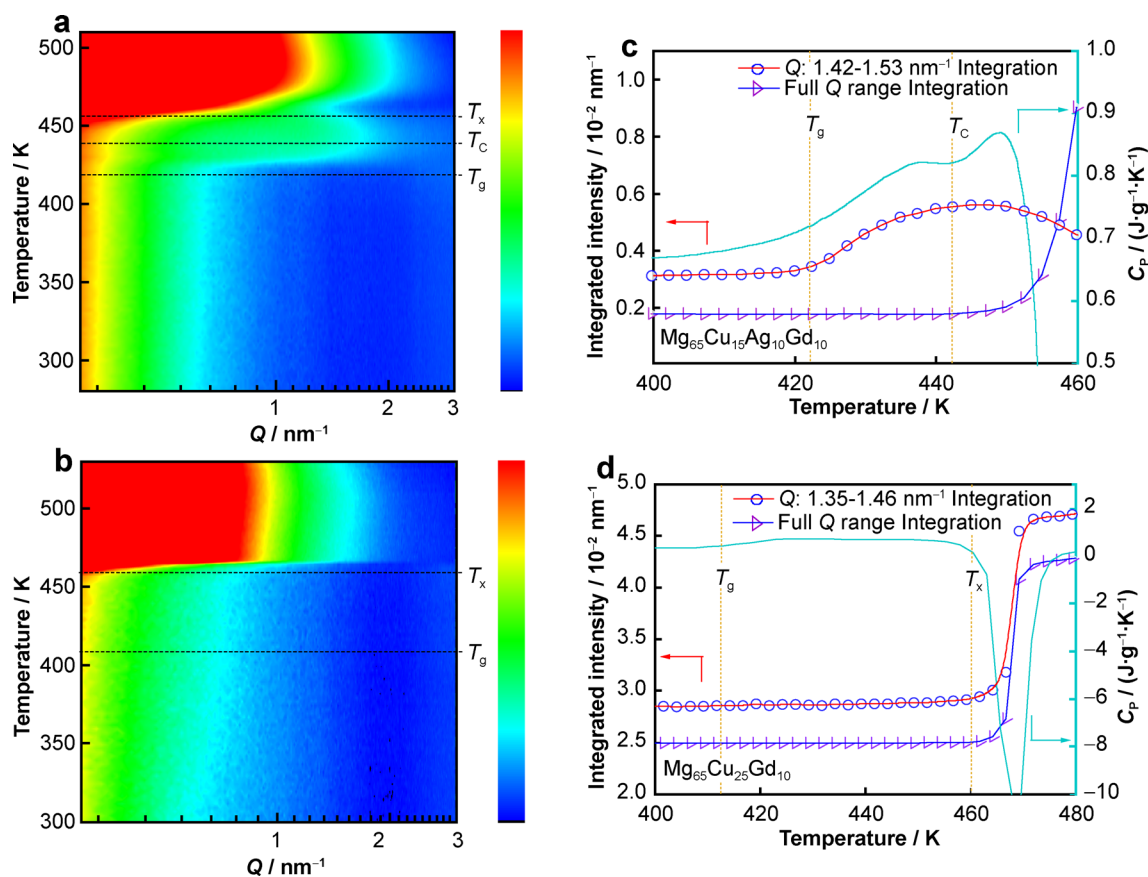
Fig. 3 SAXS profiles during heating for **a** $Mg_{65}Cu_{15}Ag_{10}Gd_{10}$ and **b** $Mg_{65}Cu_{25}Gd_{10}$ MGs; integrated SAXS intensity versus temperature during heating for **c** $Mg_{65}Cu_{15}Ag_{10}Gd_{10}$ and **d** $Mg_{65}Cu_{25}Gd_{10}$ MGs, where C_p curves have been superimposed

disappears upon heating. In contrast, $Mg_{65}Cu_{25}Gd_{10}$ does not show abnormal SAXS intensity changes during the entire heating process, as shown in Fig. 3d.

Further analysis has been performed to reveal the additional information behind the SAXS profiles related to the interface, size, and morphology of the phases during the LLPT. An interference peak appears when approaching T_C. There is an interference peak for the SAXS profile at T_C as shown in Fig. 4a, indicating the formation of the second phase with diffused interfaces. The appearance of the interference peak usually correlates with the occurrence of core–shell nano-precipitation [54]. The core–shell structure model of small-angle scattering was given by the following equation [55]:

$$I(Q) = \frac{k}{V_S}[3V_C(\rho_C - \rho_S)\phi(QR_C) + 3V_S(\rho_S - \rho_M)\phi(QR_S)]^2 \quad (1)$$

where $\phi(x) = (\sin x - x\cos x)/x^3$, R is the radius, V is the volume, and ρ is the scattering length density. The subscripts C, S, and M denote the core, shell, and matrix, respectively. k is a scale factor and $\phi(x)$ is a function that peaks at $Q = 0$ and falls monotonously at small Q values.

The core–shell model fitting analysis is shown in Fig. 4b. The characteristic lengths, including mean radius (~ 2.6 nm), shell thickness (~ 1.0 nm), reach the maximum value at T_C. The size decreases when heating above T_C, indicating that core–shell structure diminishes upon continuous heating. Moreover, the slope of the SAXS profile at the high Q region could be correlated with the shape of the second phase. A characteristic feature of the small-angle scattering from fractal scatterers and many other disorder solids often obeys a "power-law" scattering in the magnitude for two types of fractal systems, including mass fractals and surface fractals. For mass fractals, $I(q) \propto q^{-D}$, where q is the scattering vector, and D is the mass fractal dimension and has a noninteger value for random or disorder objects. For rods, disks, and spheres, D is 1, 2, and 3, respectively. For surface fractal, $I(q) \propto q^{D_S-6}$, where D_S is the three-dimensional surface fractal dimension which relates surface area [20, 56]. Figure 4c shows two power-law regimes [57], including a high q range (1.6–2.0 nm^{-1}) and an intermediate q range (0.3–0.6 nm^{-1}). At the intermediate q range, the scattering slope increases around T_C during heating, representing the metastable phase with an elongated shape appear. The slope at the high q range
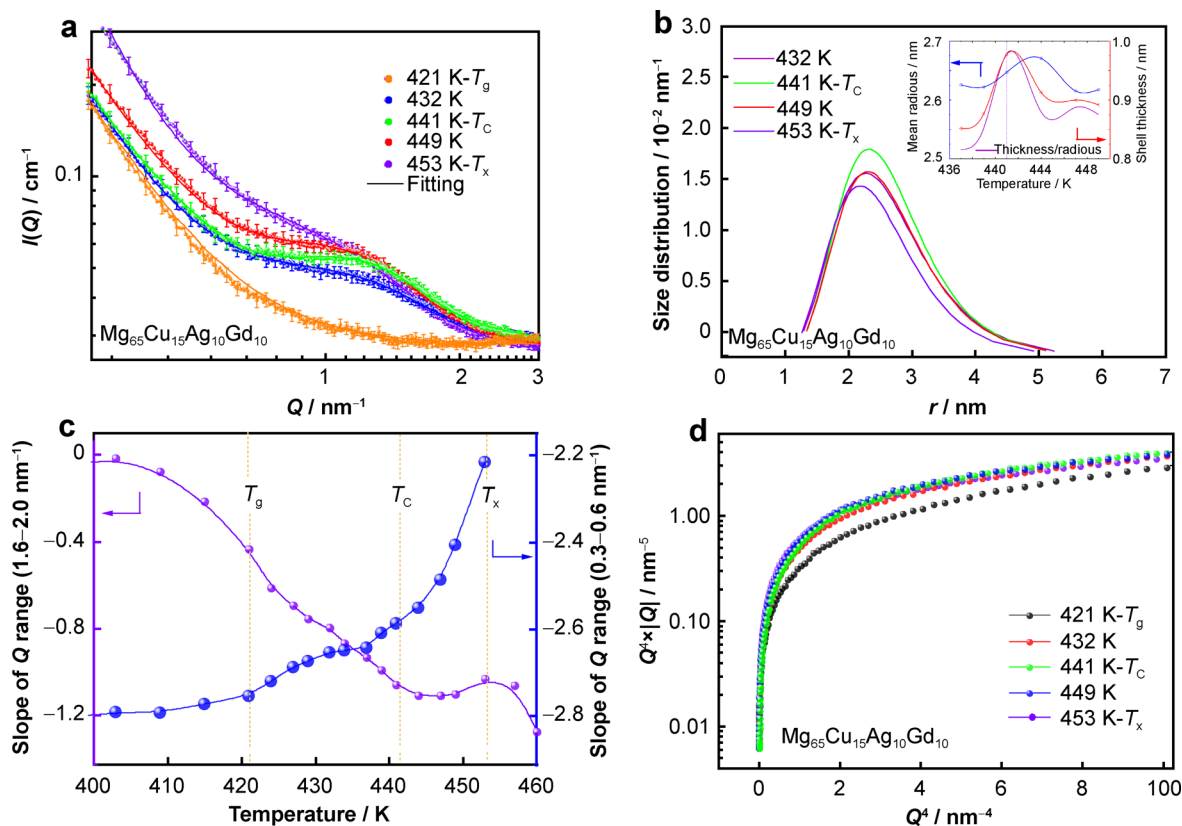
Fig. 4 a SAXS model fitting results for $Mg_{65}Cu_{15}Ag_{10}Gd_{10}$; **b** size distribution of the second phase after LLPT in supercooled liquid region of $Mg_{65}Cu_{15}Ag_{10}Gd_{10}$; **c** change of slope n values in Porod's region as a function of temperature; **d** Porod's analysis results for $Mg_{65}Cu_{15}Ag_{10}Gd_{10}$

shows a fall and rise around T_C temperature, indicating that the surface is getting smooth with the formation of the SCL2 phase and then gets rough again, which tends to have a reentrant behavior. The slope vs. temperature curve shows slope change at T_C, further confirming the occurrence of LLPT at T_C.

Figure 4d is the Porod's analysis results for the SAXS profiles at different phase transition stages. According to the Porod's law [55, 58], with the interface between the precipitates and the matrix becoming sharper, the value of $Q^4 I(Q)$ [59] tends to be more constant as Q increases to a higher value. The $Q^4 I(Q)$ at the higher Q^4 region (> 6 nm^{-4}) increases and tends to become constant as temperature increases, implying the increase in the electron density difference between the second phase and matrix, that is, suggesting that the diffused interfaces would become sharper during the LLPT and crystallization process.

3.4 Nanoindentation experiment results

Figure 5a shows the load–displacement curves of the $Mg_{65}Cu_{15}Ag_{10}Gd_{10}$ MG obtained from nanoindentation tests. It can be observed from Fig. 5a that the load–displacement curves obtained at different annealing

temperatures are different. The displacement offset gradually decreases nonlinearly with annealing temperature increasing, indicating structure changes upon annealing. According to the statistical analysis of nanoindentation experiments, Fig. 5b summarizes modulus and hardness results at different temperatures for $Mg_{65}Cu_{15}Ag_{10}Gd_{10}$. As shown by the blue curve in Fig. 5b, the slope of the modulus varies differently at different temperatures. The modulus first increases and then decreases when heating from room temperature to T_g. However, the hardness continues to increase below T_g. It seems like the relaxation process dominates and affects the mechanical properties below T_g. Moreover, in the AEP temperature region close to T_C, the modulus shows downward and upward changes. Simultaneously, there is a slope change of the hardness vs. temperature curve, indicating that the mechanical properties could also be tuned by the occurrence of LLPT and the following heat-treatment. The glass with the formation of new amorphous phases at T_C would possess higher hardness and modulus than that of a relaxing glass at $\sim T_g$. It has been found that dissimilar nanoscaled structural heterogeneity would contribute to differing creep resistance during nanoindentation tests [60]. Therefore, structural heterogeneities resulting from LLPT may play a role
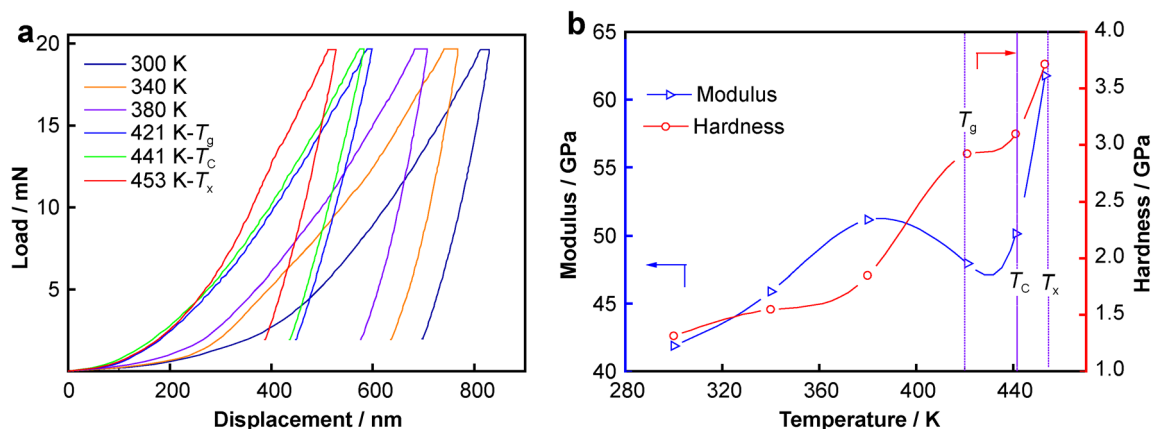
Fig. 5 Nanoindentation test results for $Mg_{65}Cu_{15}Ag_{10}Gd_{10}$ MGs: **a** load–displacement curves of $Mg_{65}Cu_{15}Ag_{10}Gd_{10}$ ribbon at different temperatures; **b** modulus and hardness as a function of annealing temperatures

in tailoring the relaxation and mechanical behaviors in Mg-based MGs.

4 Conclusion

In conclusion, multiscale structural evidence has been revealed using in situ synchrotron diffraction and time-resolved SAXS measurements. An anomalous exothermic peak and thermophysical parameters have been determined, suggesting the occurrence of an LLPT and confirming that the GFA indicators of Mg–Cu–Ag–Gd MGs are higher than those of Mg–Cu–Gd MGs. Moreover, the peak position and integrated intensity for the first sharp diffraction peak in structure factors show abnormal changes at T_C in the supercooled liquid regions of Mg–Cu–Ag–Gd MGs, indicating atomic structure evolution at medium-range order length scale when LLPT and the following reentrant supercooled liquid occurs. Square resistance measurements show consistent changes during the LLPT and the following reentrant supercooled liquid. Furthermore, the time-resolved SAXS experiment reveals a core–shell structure that emerges and diminishes when heating in the supercooled liquid region of Mg–Cu–Ag–Gd MGs, showing tunable nanoscale heterogeneity by LLPT. The morphology and interfacial information of the hidden amorphous phase resulting from LLPT have also been given. Nanoindentation experiments further confirmed that the mechanical properties could be tuned by applying appropriate heat-treatments around T_C to enable the occurrence of the LLPT. Abnormal thermodynamic behavior and anomalous structure response could not be found for the reference alloy system, Mg–Cu–Gd. The above results may suggest that the AEP, LLPT, and the following reentrant behavior correlates with the good GFA of the Ag-addition Mg-based MGs. Furthermore, it would

be interesting to determine the correlation between dynamic flow and thermodynamic phase transition in metallic glasses of an exothermic peak in the future [61]. Our results deepen the understanding of the theory of LLPT and its associated reentrant behavior and may help develop light-but-high strength Mg-based MGs of hierarchical structures from atomic-to-nanoscale.

References

[1] Tanaka H. General view of a liquid-liquid phase transition. Phys Rev E Stat Phys Plasmas Fluids Related Interdiscip. 2000;62(5): 6968.
[2] Sheng HW, Liu HZ, Cheng YQ, Wen J, Lee PL, Luo WK, Shastri SD, Ma E. Polyamorphism in a metallic glass. Nat Mater. 2007;6(3):192.
[3] Poole PH, Sciortino F, Essmann U, Stanley HE. Phase behaviour of metastable water. Nature. 1992;360(6402):324.
[4] Lacks DJ. First-order amorphous-amorphous transformation in silica. Phys Rev Lett. 2000;84(20):4629.
[5] Cadien A, Hu QY, Meng Y, Cheng YQ, Chen MW, Shu JF, Mao HK, Sheng HW. First-order liquid-liquid phase transition in cerium. Phys Rev Lett. 2013;110(12):125503.

[6] Aasland S, Mcmillan PF. Density-driven liquid–liquid phase separation in the system Al_2O_3–Y_2O_3. Nature. 1994;369(6482):633.

[7] Tanaka H, Kurita R, Mataki H. Liquid–liquid transition in the molecular liquid triphenyl phosphite. Phys Rev Lett. 2004;92(2):025701.

[8] Katayama Y, Mizutani T, Utsumi W, Shimomura O, Yamakata M, Funakoshi KI. A first-order liquid-liquid phase transition in phosphorus. Nature. 2000;403(6766):170.

[9] Soper AK, Ricci MA. Structures of high-density and low-density water. Physrevlett. 2000;84(13):2881.

[10] Zeng QS, Ding Y, Mao WL, Yang W, Sinogeikin SV, Shu J, Mao HK, Jiang JZ. Origin of pressure-induced polyamorphism in $Ce_{75}Al_{25}$ metallic glass. Phys Rev Lett. 2010;104(10):105702.

[11] Nilsson A, Pettersson LG. The structural origin of anomalous properties of liquid water. Nat Commun. 2015;6:8998.

[12] Xu W, Sandor MT, Yu Y, Ke HB, Zhang HP, Li MZ, Wang WH, Liu L, Wu Y. Evidence of liquid-liquid transition in glass-forming $La_{50}Al_{35}Ni_{15}$ melt above liquidus temperature. Nat Commun. 2015;6:7696.

[13] Lan S, Blodgett M, Kelton KF, Ma JL, Fan J, Wang XL. Structural crossover in a supercooled metallic liquid and the link to a liquid-to-liquid phase transition. Appl Phys Lett. 2016;108(21):831.

[14] Li JJZ, Rhim WK, Kim CP, Samwer K, Johnson WL. Evidence for a liquid–liquid phase transition in metallic fluids observed by electrostatic levitation. Acta Mater. 2011;59(5):2166.

[15] Wei S, Yang F, Bednarcik J, Kaban I, Shuleshova O, Meyer A, Busch R. Liquid-liquid transition in a strong bulk metallic glass-forming liquid. Nat Commun. 2013;4:2083.

[16] Georgarakis K, Hennet L, Evangelakis GA, Antonowicz J, Bokas GB, Honkimaki V, Bytchkov A, Chen MW, Yavari AR. Probing the structure of a liquid metal during vitrification. Acta Mater. 2015;87:174.

[17] Pham KN, Puertas AM, Bergenholtz J, Egelhaaf SU, Moussaid A, Pusey PN, Schofield AB, Cates ME, Fuchs M, Poon WC. Multiple glassy states in a simple model system. Science. 2002;296(5565):104.

[18] Lan S, Ren Y, Wei XY, Wang B, Gilbert EP, Shibayama T, Watanabe S, Ohnuma M, Wang XL. Hidden amorphous phase and reentrant supercooled liquid in Pd-Ni-P metallic glasses. Nat Commun. 2017;8:14679.

[19] Ge JC, He HY, Zhou J, Lu CY, Dong WX, Liu SN, Lan S, Wu ZD, Wang AD, Wang L, Yu C, Shen BL, Wang XL. In-situ scattering study of a liquid-liquid phase transition in Fe-B-Nb-Y supercooled liquids and its correlation with glass-forming ability. J Alloy Compd. 2019;787:831.

[20] Dong WX, Ge JC, Ke YB, Ying HQ, Zhu L, He HY, Liu SN, Lu CY, Lan S, Jon A, Ren Y, Wang XL. In-situ observation of an unusual phase transformation pathway with Guinier-Preston zone-like precipitates in Zr-based bulk metallic glasses. J Alloy Compd. 2020;819:153049.

[21] Xu D, Duan G, Johnson WL. Unusual glass-forming ability of bulk amorphous alloys based on ordinary metal copper. Phys Rev Lett. 2004;92(24):245504.

[22] Sohn SW, Yook W, Kim WT, Kim DH. Phase separation in bulk-type Gd–Zr–Al–Ni metallic glass. Intermetallics. 2012;23:57.

[23] Park ES, Na JH, Kim DH. Abnormal behavior of supercooled liquid region in bulk-forming metallic glasses. J Appl Phys. 2010;108(5):053515.

[24] Wang WH, Dong C, Shek CH. Bulk metallic glasses. Mater Sci Eng R Rep. 2004;44(2–3):45.

[25] Li XY, Shen YH, Cui X, Zhu PT, Zhang QD, Huang ZY, Zu FQ. The influence of casting currents on the thermal stability of the $Cu_{36}Zr_{48}Al_8Ag_8$ amorphous alloy. Cryst Res Technol. 2017;52(5):1600124.

[26] Gu J, Song M, Ni S, Guo S, He Y. Effects of annealing on the hardness and elastic modulus of a $Cu_{36}Zr_{48}Al_8Ag_8$ bulk metallic glass. Mater Des. 2013;47:706.

[27] Wang G, Guo CX, Pang SJ. Thermal stability, mechanical properties and corrosion behavior of a Mg–Cu–Ag–Gd metallic glass with Nd addition. Rare Met. 2017;36(3):183.

[28] Zhang YH, Yang T, Shang HW, Zhao C, Xu C, Zhao DL. The electrochemical hydrogen storage characteristics of as-spun nanocrystalline and amorphous $Mg_{20}Ni_{10-x}M_x$ (M=Cu Co, Mn; $x = 0$–4) alloys. Rare Met. 2013;33(6):663.

[29] Zhang M, Deng WL, Yang XN, Wang YK, Zhang XY, Hang RQ, Deng KK, Huang XB. In vitro biodegradability of Mg–2Gd–xZn alloys with different Zn contents and solution treatments. Rare Met. 2019;38(7):620.

[30] Li H, Pang S, Liu Y, Sun L, Liaw PK, Zhang T. Biodegradable Mg–Zn–Ca–Sr bulk metallic glasses with enhanced corrosion performance for biomedical applications. Mater Des. 2015;67:9.

[31] Li H, Liu Y, Pang S, Liaw PK, Zhang T. Corrosion fatigue behavior of a Mg-based bulk metallic glass in a simulated physiological environment. Intermetallics. 2016;73:31.

[32] Liu L, Teng X, Wang Y, Liu T. Glass-forming ability and crystallization of Mg-Ni amorphous alloys with Y addition. Rare Met. 2012;31(3):244.

[33] Men H, Kim DH. Fabrication of ternary Mg-Cu-Gd bulk metallic glass with high glass-forming ability under air atmosphere. J Mater Res. 2003;18(7):1502.

[34] Chrissafis K, Maragakis MI, Efthimiadis KG, Polychroniadis EK. Detailed study of the crystallization behaviour of the metallic glass $Fe_{75}Si_9B_{16}$. J Alloy Compd. 2005;386(1–2):165.

[35] Park ES, Lee JY, Kim DH. Effect of Ag addition on the improvement of glass-forming ability and plasticity of Mg–Cu–Gd bulk metallic glass. J Mater Res. 2011;20(9):2379.

[36] Ilavsky J, Jemian PR. Irena: tool suite for modeling and analysis of small angle scattering. J Appl Crystallogr. 2009;42(2):347.

[37] Zhang J, Zhang Y, Zhu B, Liu R, Li Z, Li X. Small-angle X-ray scattering investigation of aging behavior of Al-Cu-Mg-Ag alloys using synchrotron radiation. Rare Met. 2012;31(6):537.

[38] Qiu X, Thompson JW, Billinge SJL. PDFgetX2: a GUI-driven program to obtain the pair distribution function from X-ray powder diffraction data. J Appl Crystallogr. 2004;37(4):678.

[39] Li FC, Wang TY, He QF, Sun BA, Guo CY, Feng T, Yang Y. Micromechanical mechanism of yielding in dual nano-phase metallic glass. Scripta Mater. 2018;154:186.

[40] Turnbull D. Under what conditions can a glass be formed? Contemp Phys. 1969;10(5):473.

[41] Lu ZP, Tan H, Ng SC, Li Y. The correlation between reduced glass transition temperature and glass forming ability of bulk metallic glasses. Scr Mater. 2000;42(7):667.

[42] Lu ZP, Liu CT. A new glass-forming ability criterion for bulk metallic glasses. Acta Mater. 2002;50(13):3501.

[43] Liu SN, Wang LF, Ge JC, Wu ZD, Ke YB, Li Q, Sun BA, Feng T, Wu Y, Wang JT, Horst H, Ren Y, Jonathan DA, Wang XL, Lan S. Deformation-enhanced hierarchical multiscale structure heterogeneity in a Pd-Si bulk metallic glass. Acta Mater. 2020;200:42.

[44] Lan S, Wu Z, Wang XL. Multiscale structures and phase transitions in metallic glasses: a scattering perspective. Chin Phys B. 2017;26(1):17104.

[45] Yavari AR, Hamar-Thibault S, Sinning HR. On the microstructure of amorphous $Pd_{46}Ni_{36}P_{18}$ with two glass transitions. Scr Metall. 1988;22(8):1231.

[46] Binder K, Young AP. Spin glasses: experimental facts, theoretical concepts, and open questions. Rev Mod Phys. 1986;58(4):801.

[47] Lu X, Mochrie SG, Narayanan S, Sandy AR, Sprung M. How a liquid becomes a glass both on cooling and on heating. Phys Rev Lett. 2008;100(4):045701.

[48] Wang LF, Cui X, Zhang QD, Zu FQ. Thermal stability and crystallization kinetics of Cu-Zr-Al-Ag BMGs investigated with isothermal electrical resistance measurement. Met Mater Int. 2016;20(4):669.

[49] Ji YS, Chung SJ, Ok MR, Hong KT, Suh JY, Byeon JW, Yoon JK, Lee KH, Lee KS. Analysis on the phase transition behavior of Cu base bulk metallic glass by electrical resistivity measurement. Mater Sci Eng A. 2007;449:521.

[50] Lu Y, Huang Y, Wei X, Shen J. Close correlation between transport properties and glass-forming ability of an FeCoCr-MoCBY alloy system. Intermetallics. 2012;30:144.

[51] Pfeiler W. Investigation of short-range order by electrical resistivity measurement. Acta Metall. 1988;36(9):2417.

[52] Yang HW, Gong J, Li RD, Wang JQ. Thermal variation of electrical resistance of an $Al_{85}Ni_5Y_8Co_2$ metallic glass free of quenched-in nuclei. J Non-Cryst Solids. 2009;355(45–47):2205.

[53] Liu BY, Ye F. Glass transition kinetics of $La_{55}Al_{25}Ni_{10}Cu_{10}$ bulk metallic glass by electrical resistivity measurement. Rare Met. 2013;32(4):359.

[54] Yang L, Michael KM, Wang XL, Liu CT, Ma D, Jonathan A, Shi DL. Nanoscale solute partitioning in bulk metallic glasses. Adv Mater. 2009;21(3):305.

[55] Ruland WJ. Small-angle scattering of two phase systems: determination and significance of systematic deviation from Porod's law. J Appl Crystallogr. 1971;4(1):70.

[56] Putra EG, Ikram A, Bharoto, Santoso E, Fang TC, Ibrahim N, Mohamed AA. Fractal studies on titanium-silica aerogels using SMARTer. 2008; 989(1):130.

[57] Schaefer DW, Keefer KD. Structure of random porous materials: silica aerogel. Phys Rev Lett. 1986;56(20):2199.

[58] Kratky O, Porod G. Diffuse small-angle scattering of X-rays in colloid systems. J Colloid Sci. 1949;4(1):35.

[59] Wu ZD, Lu XH, Wu ZH, Kui HW. Spinodal decomposition in $Pd_{41.25}Ni_{41.25}P_{17.5}$ bulk metallic glasses. J Non-Cryst Solids. 2014;385:40.

[60] Ke HB, Zhang P, Sun BA, Zhang PG, Liu TW, Chen PH, Wu M, Huang HG. Dissimilar nanoscaled structural heterogeneity in U-based metallic glasses revealed by nanoindentation. J Alloy Compd. 2019;788:391.

[61] Ke HB, Wen P, Zhao DQ, Wang WH. Correlation between dynamic flow and thermodynamic glass transition in metallic glasses. Appl Phys Lett. 2010;96(25):51.